Application of Ultrasonic Guided Waves to Robotic Occupancy Grid Mapping

Morteza Tabatabaeipour[a*], Oksana Trushkevych[b], Gordon Dobie[a], Rachel S. Edwards[b], Ross McMillan[a], Charles Macleod[a], Richard O'Leary[a], Steve Dixon[b], Anthony Gachagan[a], Stephen G. Pierce[a]

[a] Centre for Ultrasonic Engineering, Department of Electronic and Electrical Engineering, University of Strathclyde, Glasgow G11XW, UK
[b] Department of Physics, University of Warwick, Coventry CV4 7AL, UK
[*] morteza.tabatabaeipour@strath.ac.uk

Abstract—This paper evaluates the benefits of using ultrasonic guided waves for the mapping of a structure, when implemented on a mobile magnetic robotic platform. It considers the specific problem of mapping geometric features using the guided ultrasonic waves, which enables the localisation of edges and/or the welded joints. Shear Horizontal (SH) guided waves generated by Electro-Magnetic Acoustic Transducers (EMATs) are used for mapping steel samples with a nominal thickness of 10 mm. A Bayesian mapping technique (Occupancy grid mapping) was used to map the boundaries of an irregular sample in a pseudo-pulse-echo mode. The principle is demonstrated in both simulation and laboratory-based experiments. It is shown that the proposed mapping algorithm successfully estimates the position of a sample's edges. Experimentally, a range accuracy of <1.7 mm (1σ) was achieved on a 1 x 2 m sample using miniaturised EMATs operating at a wavelength of 22 mm.

Keywords: —Automated non-destructive evaluation, guided waves, occupancy grid mapping, shear horizontal waves, ultrasonics.

1. Introduction

There is an industrial drive and statutory need to monitor the integrity and condition of industrial assets such as pipelines, tanks and vessels, in order to ensure optimum operational uptime, prevent failures and costly forced outages [1]. Non-Destructive Evaluation (NDE) is an effective method to assess the structural integrity of these assets and identify any degradation, deviations or defects. Suitable NDE techniques require precise detection, location and measurement of structural parameters such as corrosion and thickness, in a nonintrusive manner, with the results utilised to make informed decisions on future operational activities and maintenance.

Automation of NDE offers the potential to address some of the limitations of traditional manual NDE, which suffers from slow inspections, increased costs to ensure inspection safety, inconsistent measurements through poor human repeatability and an inability to access certain hazardous locations [2]. Research in automated and robotically deployed NDE seeks to address these limitations and obtain a decrease in inspection time and cost, while improving inspection accuracy and safety [3].

The current state of the art automated NDE seeks to combine inspection modalities such as ultrasonic [3,4] vision [5], optical [6] and electromagnetic [7,8] sensing techniques with robotic platforms and data analysis and interpretation software, to enable fast and intelligent inspection [9].

Ultrasonics is an inspection technique that utilises acoustic waves of frequency 20 kHz or greater to inspect industrial assets through wave propagation and analysis of parameters such as time-of-flight and amplitude [10]. Ultrasonics is a safe and sensitive inspection modality capable of measuring asset parameters such as through wall thickness, corrosion loss and weld cracking [11]. Current state-of-the-art industrial ultrasonic NDE implemented on robots [3,12] typically measures component thickness and corrosion through the use of normal incidence bulk wave inspection, directed perpendicularly into the subject surface [13]. These waves are typically generated using single-element or phased array bulk wave transducers, which require contact with the sample. Although quicker and cheaper than manual NDE, such approaches are still time-consuming as the probes are required to be scanned across the full area to achieve the desired coverage [4]. Furthermore, such systems typically estimate their position using wheel encoders, which drift over time, especially when not travelling in a straight line [14]. There are limited localisation systems available that provide the appropriate level of global accuracy (~10mm) and those that do exist, such as Laser Trackers [15], are prohibitively

expensive (2-3x the cost of inspection robots).

Combining medium-range inspection techniques with on-board localisation, both using ultrasonic guided waves, can improve automated inspection using robotics in these two key areas. This paper describes such an advance.

1.1. Ultrasonic Guided Waves

The point-by-point inspection manner of state-of-the-art crawlers is suitable for defect identification, but not detection of the boundaries or the welded regions, and hence cannot be used for robot localisation and mapping of an unknown component. Bulk waves also cannot be used for assessing areas with limited access, such as defects under support; however, guided waves are capable of doing that. The reason is that the bulk waves only propagate in the thickness direction of the component; whereas guided waves propagate across the sample following its top and bottom boundaries [16,17]. Concisely, a crawler equipped with bulk wave inspection needs to move across large portions of the sample in small step iterations of measurement positions to inspect a significant area, however, a system equipped with guided wave generation methods can map a large portion of the sample and the geometrical features with limited, sparsely spread measurement positions. Therefore, measurements using bulk waves are time-consuming compared to the guided waves.

Guided wave inspection is a relatively well-established non-destructive-testing (NDT) technique that has found the most success in long-range pipe inspection, where it is deployed from a fixed ring/collar of sensors as discussed in detail in Ref [16,18]. Guided waves have also been used in structural health monitoring using a sparse array of fixed transducers [16]. However, they are primarily used for defect detection, and have not been utilised as the sensory input for robotic mapping previously. When coupled with automated deployment, guided waves can inspect large complex assets to rapidly inspect the structure [19] , while signal processing approaches can be utilised to improve local spatial resolution and defect sensitivity [20]. Note that [19] only inspects the area under the robot using a non-probabilistic local pitch-catch technique (like traditional NDT). Ref [20] proposes longer range propagation (like this work), but uses a traditional NDT/Radar algorithm (Synthetic aperture focusing technique). In this work, we transition to a robotic algorithm (OGM) more suited to live NDT data processing.

1.2. Autonomous Environmental Mapping

Environmental identification and mapping of surrounding features and regions are essential for successful autonomous NDE. Tasks such as localisation, navigation and collision avoidance, which are essential in order to achieve full desired area coverage, require suitably accurate and well defined local environment maps [21,22]. Occupancy Grid Mapping (OGM) is a probabilistic Bayesian mapping technique developed to map unknown and unstructured environments [23,24]. OGM typically utilises data and measurements from range sensors such as airborne ultrasonic distance transducers [25], Light Detection And Ranging (LiDAR) [26], Radio Detection Ranging (RaDAR) [27], vision-based ranging [28] and/or fusion of all on-board sensor measurements [29] to generate the resultant map. When considering traditional large-scale industrial assets, materials, surface conditions and density of neighbouring features often limit the applicability and accuracy of these sensors [30].

1.3. Guided Wave-Occupancy Grid Mapping (GW-OGM)

This body of work presents the novel concept, research, and developments of a Guided Wave-Occupancy Grid Mapping (GW-OGM) strategy for rapid automated NDE of large industrial structures. GW-OGM can utilise reflections from structural boundaries, weldments and asset features to map the environment under inspection and provide data for robot path planning and localised inspections. In principle, using ultrasonic guided waves for occupancy grid mapping is beneficially two-fold as:

- Automated corrosion mapping looks to build a 2D thickness map of the surface of a structure, mapping areas of corrosion. This lends itself well to an OGM implementation and guided waves let us cover large areas quickly compared to bulk ultrasound.
- Using guided waves, we can localise the robot relative to the structure rather than the external geometry that would be detected by a LIDAR or camera system. This removes sensitivity to the external environment or its lighting.

As a result, by using guided waves we can simultaneously localise and map internal features of an unknown component for NDE purposes.

The concept of using ultrasonic guided waves as a sensing modality is highly advantageous when considering large-

scale industrial asset inspection, as it can be utilised to provide both the mid-range, large area mapping sensor input capability for OGM, but also for NDE screening of the components requiring inspection. Furthermore, ultrasonic guided wave propagation is well developed and understood in large-scale industrial asset inspection materials such as carbon steels [16]. While combining mobile robotic systems and ultrasonic inspection is not new ([4,19,31]), the concept presented in this paper of utilising ultrasonic guided waves as the input for a mapping does represent an advancement of the state-of-the-art for robotic NDE. In other words, the novel contribution of this paper is the development, characterisation and demonstration of a new ranging sensor based on EMAT generated guided waves. These new ranging sensors are integrated into an OGM algorithm for mapping the internal features of an industrial component, such as storage tanks. The process of generating maps is crucial to understanding the surrounding regions of a structure under examination when an inspection crawler navigates on an unknown component. The robot should be able to autonomously construct a map of a component using onboard inspection sensors.

Although guided waves can be explored for localisation of the robot, mapping, and NDT (i.e., defect detection) of a component, this research paper merely investigates the latter one. The localisation of such crawlers is also useful to locate the inspection data. Conventional ranging sensors like LIDAR and airborne ultrasonics, require extra hardware and external reflective surfaces, which is not usually available. Therefore, guided waves can be an alternative technique for estimating the position of the robot as well. The specific novelty of the paper can be summarised as follows:

1. Characterisation of an SH guided wave ranging sensor developed using EMAT technology.
2. Creation of a sensor model for the new transducer/wave mode.
3. Demonstration of the sensors integrated into an OGM algorithm.

The remainder of this paper is organised as follows: Section 2 provides a background on the theory of guided waves, method of generation and the choice of wave mode, as well as introducing Occupancy Grid Mapping. Section 3 presents the Finite Element Analysis (FEA) model that was implemented in order to simulate the GW-OGM concept on a representative industrial geometry. Section 4 covers the experimental evaluation of the system as well as the sensitivity of guided waves to representative geometrical features on the industrial geometry. Section 5 concludes this paper and notes the limitations of the proposed GW-OGM as well as future areas of relevant work.

2. Sensor and Mapping Concepts

2.1. Shear Horizontal (SH) Guided Waves

Guided waves include Lamb waves and Shear Horizontal (SH) waves. SH waves oscillate perpendicular to the propagation path, and have particle motion in the transverse plane, while Lamb waves have particle vibrations in the sagittal plane [16]. The transverse polarization of SH wave modes may enhance the sensitivity of this type of guided wave to certain types of structural features such as welded regions, as well as the sensitivity to defects oriented parallel to the wave vector [32,33].

SH waves are complicated to generate using piezoelectric transducers, but can be generated in metals using electro-magnetic acoustic transducers (EMATs). EMATS use a combination of a pulsed current and a magnetic field to generate or detect a disturbance in the metal lattice, which propagates as an elastic wave [34]. Unlike traditional piezoelectric transducers, they do not require couplant, which simplifies deployment on a robotic platform [33]. However, the magnetic field can cause difficulties when scanning magnetic materials. In this work, we used miniaturised periodic permanent magnet (PPM) EMATS which consist of a racetrack-shaped coil and an array of permanent magnets spaced to match the SH wavelength -for more discussion of the design see Ref [35]. PPM EMATS/SH waves are being used increasingly for NDE applications as SH waves scatter from both perpendicular and parallel defects relative to the wavefront [33], [36,37] . It has also been reported that SH_1 wave modes are sensitive to wall thinning damage due to the dispersive behaviour of this wave mode [38–40].

The multimodal and dispersive behaviour of SH guided waves on a 10mm thick steel sample is shown in Fig. 1, calculated using GUIGUW [41]. The dispersion diagram shows that the group velocity (the velocity at which the energy of the wave modes is conveyed along the plate) for most of the modes is a function of frequency; if a particular dispersive wave mode is excited, the different frequency components of the excited wave will travel at different velocities. Velocity of these modes also depends on the thickness of the sample. Practically, using dispersive modes means additional data processing [42] is required to see geometric features as reflections of waves at different velocities blur the ability to easily identify feature reflections from noise, depending on the level of dispersion this can be a difficult task.

The SH$_0$ mode is the only non-dispersive wave mode so will be used in this research, as the velocity does not depend on frequency or sample thickness, and hence spurious distance results will not be obtained if the sample thickness varies. Secondly, this will make the identification of reflections simpler as they will be easily identifiable. The frequency of operation is chosen based on the wavelength introduced by the PPM array layout.
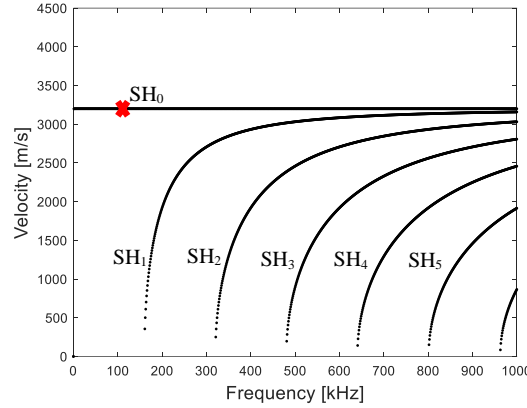

Fig. 1. Group velocity dispersion curve for a 10 mm thick steel sample, showing that SH$_0$ is a non-dispersive wave mode. Note that the red star shows the wave mode and frequency used in this paper.

2.2. Occupancy Grid Mapping (OGM)

OGM refers to a probabilistic algorithm in the field of mobile robots which addresses the problem of generating maps from noisy and uncertain sensor measurement data (in this work, guided waves are used as sensory input), with the assumption that the robot pose is known [43].

Conceptually the OGM simply partitions a 2D environment into cells with each being the probability of three states including free, occupied, and unknown. Values close to 1 (black) represent a high probability that the cell contains an obstacle (in this work, obstacle refers to the geometrical features of a component such as edges/welded regions). Values close to 0 (white) represent a high probability that the cell is obstacle-free. As the robot drives around learning the environment, the unknown cells are filled in. Bayesian probability is then used to update probabilities when the new measurements are taken for any given cell. Information about which areas are unknown is also important, e.g., for autonomous exploration of an environment. The mathematical formulation of the OGM algorithm is discussed in the following paragraphs.

In OGM, sensor readings are transformed into probabilities and then combined using Bayes' rule for data fusion [43]. A standard occupancy grid map calculates the posterior over the map $p(m_i| z_{1:t}, x_{1:t})$ given a set of measured data up to time $(z_{1:t})$, and the robot poses$(x_{1:t})$, which are assumed to be known, and part of the measurement here. The individual grid cells are labelled m_i. By transforming the measurement into a global coordinate system, the robot pose information can be incorporated into the measurement and the pose itself does not provide any additional information about the environment, meaning that we may omit the pose information$(x_{1:t})$ [43], so that:

$$p(m_i|z_{1:t}, x_{1:t}) = p(m_i|z_{1:t}). \tag{1}$$

In principle, the posterior probability is the probability that an event will happen after taking into consideration all new and previous information. Note that the following posterior probability is estimated by updating the prior probability using Bayes' rule, as briefly is discussed in Appendix A.

$$p(m_i|z_{1:t}) = \frac{p(z_t|m_i, z_{1:t-1}) \, p(m_i| z_{1:t-1})}{p(z_t| z_{1:t-1})}, \tag{2}$$

where m_i is the occupancy of the grid cell in the (x,y) position. In standard OGM, for the sake of simplicity, it is assumed that the occupancy of individual grid cells m_i is independent of the occupancy of neighbouring cells [21].

Therefore, we can make the Markov assumption on $p(z_t|m_i, z_{1:t-1})$. In this case, the Markov assumption means that if we know the state of the robot and were interested in predicting the measurement z_t, past measurements would provide us with no additional information. In mathematical terms, this is expressed by the following equation:

$$p(z_t|m_i, z_{1:t-1}) = p(z_t|m_i) \tag{3}$$

We then expand the equation (2) once again by applying Bayes' rule on the right side of equation (3) and plug it back into equation (2). $p(m_i|z_{1:t})$ is now based on the inverse sensor model $p(m_i|z_t)$. The inverse sensor model specifies a distribution over the map as a function of the measurement. As a result, to calculate the log odds representation of occupancy grid mapping, the odds of equation (2) can be expressed as:

$$\frac{p(m_i|z_{1:t})}{p(\overline{m}_i|z_{1:t})} = \frac{p(m_i|z_t)\,p(\overline{m}_i)p(m_i|\,z_{1:t-1})}{p(\overline{m}_i|z_t)p(m_i)p(\overline{m}_i|\,z_{1:t-1})}, \tag{4}$$

where $p(\overline{m}_i|z_{1:t})$ is the complement of the $p(m_i|z_{1:t})$. By taking the log of expression (4) and formatting it as follows:

$$\log\frac{p(m_i|z_{1:t})}{p(\overline{m}_i|z_{1:t})} = \log\frac{p(m_i|z_t)}{p(\overline{m}_i|z_t)}\,\log\frac{p(m_i|\,z_{1:t-1})}{p(\overline{m}_i|\,z_{1:t-1})} - \log\frac{p(m_i)}{p(\overline{m}_i)}, \tag{5}$$

the log-odds representation of occupancy grid mapping algorithm, equation (4), can be formulated as [25,43]:

$$l(m_i|z_{1:t}) = l(m_i|z_t) + l(m_i|z_{1:t-1}) - l(m_i), \tag{6}$$

where $l(m_i|z_t)$, $l(m_i|z_{1:t-1})$, and $l(m_i)$ are the inverse sensor model, recursive term and prior map, respectively. As a result, OGM can be formulated as shown in Algorithm 1. Line 8 of Algorithm 1 shows how the posterior probabilities are finally recovered from the log odd ratio.

In principle, OGM is usually described using two algorithms, see Algorithms 1 and 2. The former describes the main part of the OGM, and Algorithm 2 (also shown in Fig. 8) formulates the inverse sensor model of the OGM algorithm. The inverse sensor model enables the system to estimate occupied, empty and unknown regions given the sensor measurements. The further details of the inverse sensor model will be explained in section 3.2. Note that MATLAB software was used for the implementation of the OGM algorithm.

---

lgorithm 1: Occupancy Grid Mapping

Inputs: Position of the robot (x_t), range (z_t), prior map $(l_{t-1,i})$
Output: Occupancy grid map
1: **For** all grid cells, m_i do
2:   **If** m_i in perceptual field of z_t then
3:     $l_{t,i} = l_{t-1,i}$ + Inverse Sensor Model $(m_i, z_t) - l_0$
4:   **Else**
5:     $l_{t,i} = l_{t-1,i}$
6:   **End**
7: **End**
8: $p(m_i|z_{1:t}) = \frac{e^{\,l_{t,i}}}{1+e^{\,l_{t,i}}}$

---

3. Finite Element Based Simulation

Finite Element Analysis (FEA) using OnScale software suite (OnScale, Redwood City, CA) [44] was used to generate synthetic ultrasonic signals on which to develop and demonstrate the OGM algorithm. OnScale was selected as it is a time-domain mixed explicit/implicit FEA programme, which makes it a fast and memory-efficient tool for solving large-scale 3D models in the time domain [45,46].

A 10 mm thick mild steel sample representative of industrial structures such as storage tanks was simulated, with its geometry and dimensions shown in Fig. 2a. A square hole with dimensions of 20 x 20 cm and an angled cut were added to create a more complicated geometry for a better assessment of the GW-OGM solution.

A PPM EMAT generator [35] with a 25 mm wavelength and two detectors positioned 5 cm apart were included in the model, as shown in the schematic in Fig. 2b. In order to build the required dataset to map the extent of the plate using the SH_0 mode, multiple simulations were executed with the position of the simulated EMATs translated around the sample to provide the required coverage of the plate as shown in Fig. 2a with the yellow dashed line. The EMAT generator was modelled as an in-plane loading force on the inspected sample under each dummy magnet in the PPM array (6-row coloured boxes, see Fig. 2b). Since the OGM works better when more data is available, three different EMAT arrangements (sending waves in directions 0°, 90° and 45° relative to the sample left edge) were tested, as

information from all three tests would supply data to the map, see Fig. 3. In practice, either the sensor head needs to rotate to point in these directions, or three sets of EMATs in different arrangements should be mounted on the robot. Note that for more complex shape structures, more EMAT arrangements should be considered for the GW-OGM technique as the ultrasonic wave does not reflect back towards the generation point when the target surface is not perpendicular to the wavefront vector.
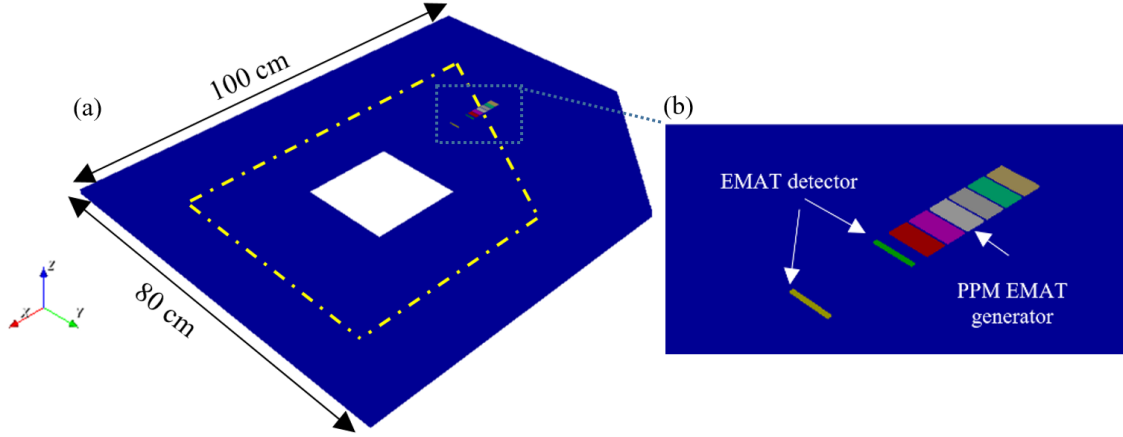

Fig. 2. (a) A simulated 10 mm thick steel sample. (b) Arrangement of PPM EMAT generator and detectors orientated at 90 degrees to the y-axis. Note that the yellow dashed line indicates the position of the robot where measurements are made. The signals are measured at every 1-2 cm increment.
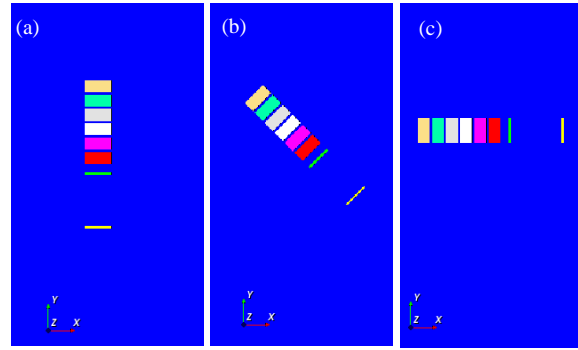

Fig. 3. EMAT arrangements to measure the signals in three different directions in each position, a) 0°, b) 45°, c) 90°
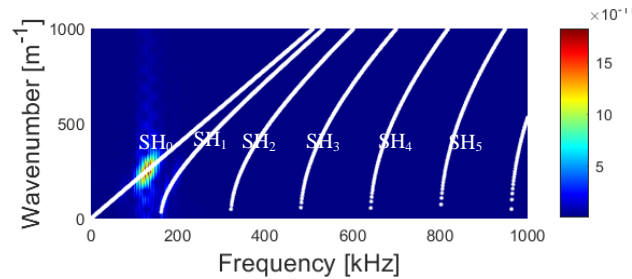

Fig. 4. Frequency-wavenumber image of simulated data, overlaid on the theoretical calculations (white solid lines) to validate the simulation results, showing that SH_0 is generated.

In general, signals are measured in both the *x*- and *y*-directions in OnScale, defined in Fig. 2a. Therefore, a rotation matrix was used to calculate the normal and tangential components of signals measured at φ=45° degrees:

$$\begin{bmatrix} S_\varphi \\ S_{90-\varphi} \end{bmatrix} = \begin{bmatrix} cos(\varphi) & -sin(\varphi) \\ sin(\varphi) & cos(\varphi) \end{bmatrix} \begin{bmatrix} S_x \\ S_y \end{bmatrix}, \tag{7}$$

where S_x and S_y are measured signals in the x and y directions.

A four-cycle sine wave tone burst signal at 128 kHz was fed into the EMAT generator in order to generate SH_0 waves. The generation of this desired mode in the simulation was further validated by overlaying the theoretical

frequency-wavenumber graph on the one obtained from the simulated data using a 2D-FFT analysis [47,48], with results shown in Fig. 4.

In order to calculate 2D-FFT, the in-plane signals are initially measured with a 1mm increment step size along the SH propagation path. The acquired signals are then processed using a 2D-FFT to obtain a frequency-wavenumber (*f-k*) image. The 2D-FFT of a function $f(x,t)$ can be defined as [16]:

$$H(k,f) = \left| \iint f(x,t)\, e^{-j(wt+kx)} dx dt \right|,\tag{8}$$

where $f(x,t)$ here contains the measured signals on the plate in the time-distance (*x-t*) domain. w and k are the angular and wavenumber, respectively.

3.1. Range and Direction Estimation

Calculation of the range requires knowledge of the wave properties. The directivity pattern of a PPM EMAT transducer indicates that the wave propagates symmetrically in both the forward and backward directions, confirmed by the data shown in Fig. 5, [49]. The directivity pattern of the fabricated EMATs were also experimentally evaluated as shown in Fig. 6 of ref [50] by the authors; techniques have been reported to suppress the unwanted direction [51], but in this work, we used two EMAT receivers to identify forward and backward travelling waves.
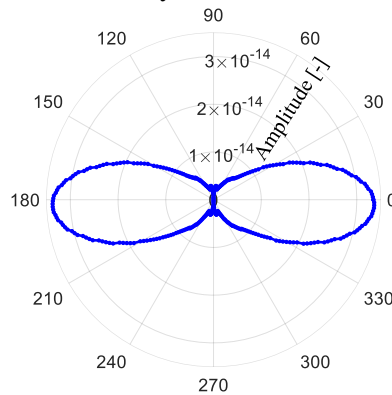

Fig. 5. Directivity pattern of a PPM EMAT measured at the far-field (75 mm from the PPM EMAT centre). Note that the radius and theta axes indicate the amplitude of the measured signals and the angle relative to the EMAT direction, respectively.

This bidirectional characteristic of the waves generated by PPM-SH EMATs makes it difficult to interpret which side of the sample is the source of the resulting echo; however, this information is needed for OGM in addition to the range. Therefore, one generator and two detectors are used (Fig. 2b), and echo directions are calculated by a comparison between the Time of Flight (ToF) of the first echoes detected by each EMAT detector. Fig. 6 illustrates how the direction of the first arrival echo is estimated using two detectors. *T1* and *T2* stand for the arrival times of the first echoes received by detector 1 and detector 2, respectively. If *T1<T2* the first echo is bouncing off the right reflector (see Fig. 6a), however, if *T1>T2*, it is reflected off the left edge (see Fig. 6b). Due to this bidirectional characteristic of EMATs, the two first echoes of a measured signal are reflected from close and far features/edges, respectively if the wave vector is perpendicular to both close and far features of the component.
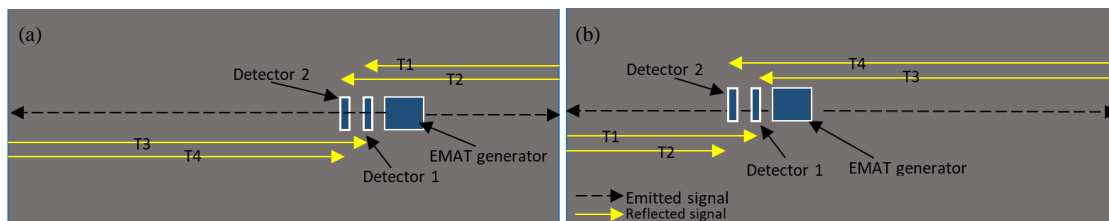

Fig. 6. A schematic image for estimating the direction of first arrival echo using two detectors. T1 and T2 stand for the first echoes received by detector 1 and detector 2, respectively.

As the simulated robotic crawler moves around the sample, the detected signals are processed. The received signals

are first bandpass filtered in the range of 50-200 kHz and then they are cross-correlated with the excitation signal, a four-cycle sine wave tone burst signal at 128 kHz, as follow:

$$R_{ES}(t) = \int_{-\infty}^{+\infty} E(\tau)S(t+\tau)d\tau, \tag{9}$$

where $E(t)$ and $S(t)$ are the excitation signal and the filtered signals respectively.

Then, the envelope of the cross-correlation signal is obtained using the Hilbert transform as follows:

$$H(R_{ES}(t)) = \frac{1}{\pi}\int_{-\infty}^{+\infty}\frac{R_{ES}(\tau)}{t-\tau}d\tau, \tag{10}$$

$$Env(t) = |S(t) + i\,H(R_{ES}(t))|, \tag{11}$$

where $H(R_{ES}(t))$ and $Env(t)$ are the Hilbert transform of the cross-correlated signal and the envelope of the signal respectively. Note that the envelope is defined as the magnitude of the complex formulation of the signal, which is also known as the analytic signal.

The detected envelope is then normalized to the amplitude of the direct signal as shown in Fig. 7a. Finally, the local maximum indices of the envelope function are selected as the arrival time of desired reflected echoes from the close and far edges of a given sample as shown in Fig. 7b. It is important to note that a group velocity of 3200 m/s, corresponding with the group velocity of SH_0 wave mode at the excitation frequency, was considered for estimating the ranges. This can be calculated by the group velocity dispersion curve analysis [16].

Transducers need to be placed close to the generator for the small sample modelled here. When this is the case in experiments, the direct waves are not observed as they are in the so-called dead zone of the amplifier, which covers the initial time period of the data in Fig. 7. The length of the dead zone depends on the electronics and impedance of the transducers as well as excitation frequency and the number of cycles. Ideally, the detectors should be placed apart so that the direct signal should be always observed as an indicator that the system is working as expected.
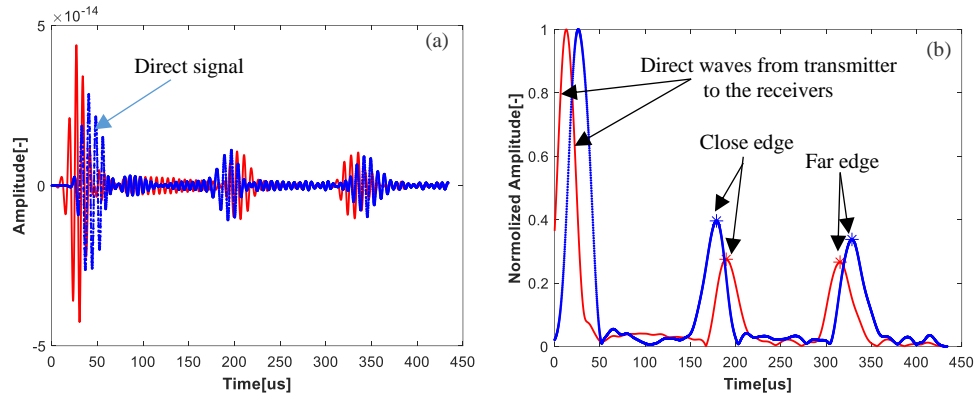

Fig. 7. A typical measured signal in a position where EMATs are arranged perpendicular to two parallel reflectors (edges). (a) Raw data. (b) Processed data. Note that this is measured signals using two EMAT detectors.

3.2. GW-OGM Algorithm

In each EMAT and wave propagation direction (0°, 90° and 45°), up to two (zero, one or two) echoes are extracted depending on the angle of EMAT transducer relative to the reflector. If there is no echo detected above a set wave amplitude threshold (either there is no reflector, or the echo has an amplitude below the threshold) the algorithm assumes there is nothing there. However, when an echo is above the threshold, the algorithm, which uses a conic shape sensor model as shown in Fig. 8a, assumes the area before the echo is clear, and the echo area is occupied.

The inverse sensor model for the pulse-echo mode is formulated in Algorithm 2 and illustrated in Fig. 8. Three regions, namely unknown (I), occupied (II) and free (III) regions, are defined in the model. As the unknown region's name suggests, there exists no information about this region. Therefore, cells in the area I remain as before when the

GW-OGM is updating the map information. However, the occupied zone is a region with the highest likelihood of a reflector's position. In contrast, the free zone is the area between the EMATs and that reflector (region II) with the lowest probability of any reflector's presence.

The distance and relative angle of each grid cell to the EMAT generator and the main acoustic axis (EMAT direction) are respectively calculated. This information is further utilized to map each cell into one of the occupied, free and unknown regions. Note that the grid resolution of 1000 cells per meter was taken into account for the GW-OGM algorithm.

A non-uniform distribution was used for occupied and free regions as shown in Algorithm 2, lines 6 and 8, respectively. A Gaussian distribution was selected for the occupied regions, as shown in Fig. 8b. Its normal distribution parameters were calculated according to a fitting of the directivity shown in Fig. 9b, indicating that the likelihood increases as the elements get closer to the centre of the occupied region. In the free region, the ($(z_{max} - r)/z_{max}$) term indicates that closer elements to the EMAT generator have the minimum likelihood. Moreover, the (($\beta - \theta)/\beta$) term signifies that the grid cells that are close to the main lobe (acoustic main axis) have the minimum likelihood in the free region, see Fig. 8. Note that region II has a finite thickness (α) that depends on the accuracy of the range measurement.

Algorithm 2: Inverse Sensor Model

Inputs: Pose of the robot (x_t), range (z_t), individual cell (m_i), measurement direction (θ), maximum range (z_{max}), width of occupied region (α)

Outputs: The probability of each cell in the map

1: $r = \sqrt{(x_i - x)^2 + (y_i - y)^2}$

2: $\emptyset = atan2(y_i - y, x_i - x) - \theta$

3: **If** $r > min(z_{max}, z_t + \alpha/2)$ or $|\emptyset - \theta| > \beta$ **then**

4:      $return \{ l_0 \}$

5: **Elseif** $z_t < z_{max}$ and $|r - z_t| < \alpha/2$

6:      $return \{ e^{-(\emptyset - \theta)^2/2\sigma^{\wedge}2} \}$

7: **Else**

8:      $return \{ -((\frac{z_{max} - r}{z_{max}}) + (\frac{\beta - \theta}{\beta}))/2 \}$
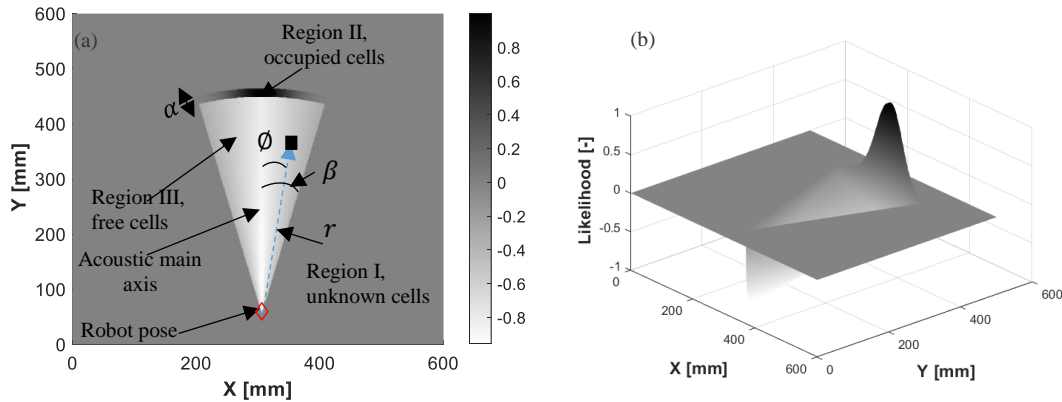
9: **End**

Fig. 8. An example of an inverse measurement model, see Algorithm 2.
(a) 2D representation. (b) 3D representation.

In order to estimate this model, three input parameters are required, the direction of the received echoes (θ), the maximum range of SH$_0$ wave mode (z_{max}) and the half angle representing the field of view of SH$_0$ wave mode (β). With knowledge of the EMAT arrangement, the desired echo direction (θ) can be estimated as explained in section 3.1. In general, the range of guided wave propagation can be divided into three categories of short-range (<<1m), medium-range (up to about 5m) and long-range (up to around 100m) [18]. The maximum range mainly depends on the wave mode, excitation frequency, material and the measurement system, which may consequently influence the signal to noise ratio (SNR) of the reflected echoes. Given all these factors, we could confirm that SH$_0$ wave mode can propagate up to three meters using our miniaturized EMATs, as will be explained in section 4.2. The maximum range should be adjusted if one of the influencing parameters varies. For instance, the dispersive SH$_1$ wave mode may be significantly distorted after propagating long distances compared to the non-dispersive SH$_0$, which makes it more challenging to find the correct ToF value.

The β parameter can be inferred by calculating the amplitude of the monitored signals generated by the EMAT as a function of angle in the far-field of the transducer (measured at 1m) as shown in Fig. 9a. The half-power beamwidth (-3 dB) of the main lobe was considered as the field of view of the SH_0 wave mode, see Fig. 9b. Note that the β parameter mainly depends on the wave mode, the wavelength and the transducer aperture length.

Fig. 10 illustrates the process of constructing the OGM, showing the accumulated data and map produced at three different time instances. Any arbitrary path with full coverage can be selected, however, this straight-line movement, see Fig. 2a, was chosen to reduce the accumulated error of the robot's drifting and for simplicity of control in practice [4,52].

As mentioned in section 3.1, the signals are measured at 0°, 45° and 90° (robot pose shown in Fig. 10c), and up to two available echoes are considered while the EMATs are mobile. Therefore, one can notice that, as the robot passes the corridor area (shown in Fig. 10b) multiple sample edges are mapped as the OGM takes advantage of both forward and backward echoes of the EMAT sensors. This advantage eliminates any need for altering the robot's heading or installing another sensor needed to generate waves in the opposite direction. Any error in the estimation of ToF may cause some spurious occupied regions to be recorded, such as those indicated in Fig. 10a. Note that the unknown regions are represented by grey, which can be recognised as an area for further navigations or areas outside of the sample edges.
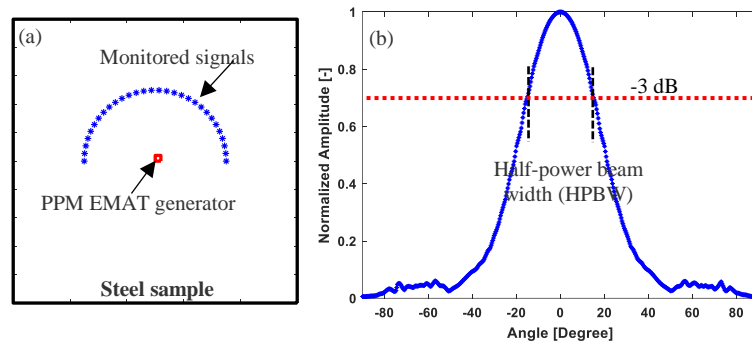

Fig. 9. EMAT amplitude as a function of angle calculated in the simulation to estimate the beamwidth of the EMAT. (a) Measurement setup. (b) amplitude-angle graph.
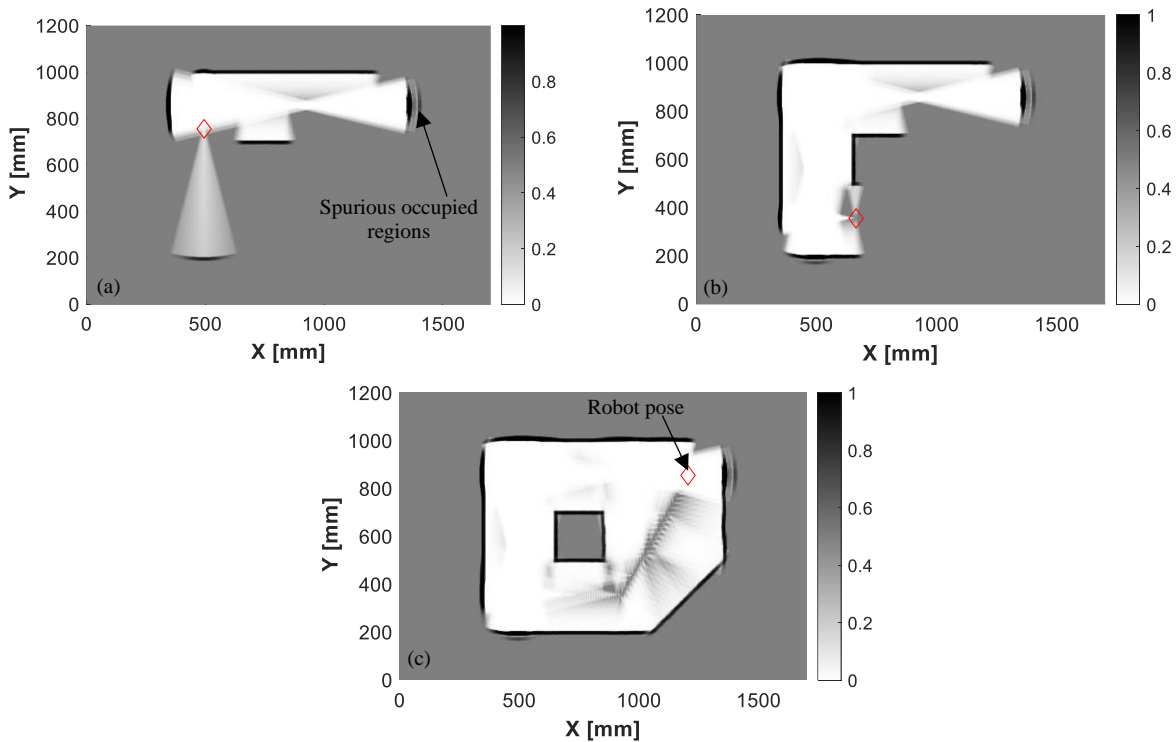

Fig. 10. Occupancy Grid Mapping at three instances, illustrating that OGM is able to estimate the specimen's geometrical features. (a) t_{57}. (b) t_{115}. (c) t_{190}. Note that the grid resolution for this mapping is 1000 cells per meter.

4.   Experimental Analysis

Two experiments were carried out on a rectangular 10 mm mild steel sample (S275) containing a butt-welded region to evaluate the sensitivity of SH wave modes to geometrical features of a welded sample and gives a validation of the GW-OGM algorithm. For all measurements, a RITEC RPR-4000 Pulser/Receiver (RITEC Inc., Warwick, RI) [53] was used to generate a 4-cycle tone-burst at the desired frequency. The reflected signals were then measured using a PicoScope 5000a series (Pico Technology, Cambridgeshire, UK) [54], which was triggered by the RITEC. All the measuring equipment was controlled by a LabVIEW [55] based programme, see Fig. 11. Two sets of EMATs were used: a commercial pair from Sonemat, with model numbers SHG2541-S and SHD2541-S, with nominal wavelength of 25mm, and a miniaturised set of a generator and two receivers with a nominal wavelength of 22mm [50]. PPM EMATs have a large number of magnets leading to magnetic attraction forces over 200kg for the wavelengths used. This makes deployment on small robots very difficult, when assessing ferritic steel samples. Miniaturisation was done to reduce magnetic drag on ferritic samples and bring it into the operational range for the robot [50].
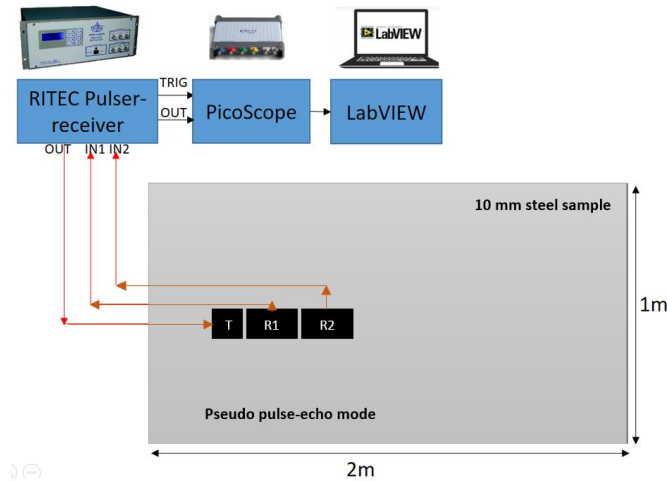

Fig. 11. Experimental setup to validate GW-OGM. T, R1, R2 stand for EMAT transmitter, EMAT receiver 1 and EMAT receiver 2.

4.1. Sensitivity of SH wave modes

The sensitivity of SH wave modes to structural features was tested using the commercial PPM EMAT transducers from Sonemat Ltd. (Sonemat, Coventry, UK) [56] with a 25 mm wavelength, with the set-up shown in Fig. 12a. The EMATs were placed side by side at the edge of the plate. The dotted black and solid yellow lines show the propagation path from the EMAT generator to the butt-welded region and the right edge of the sample, respectively.
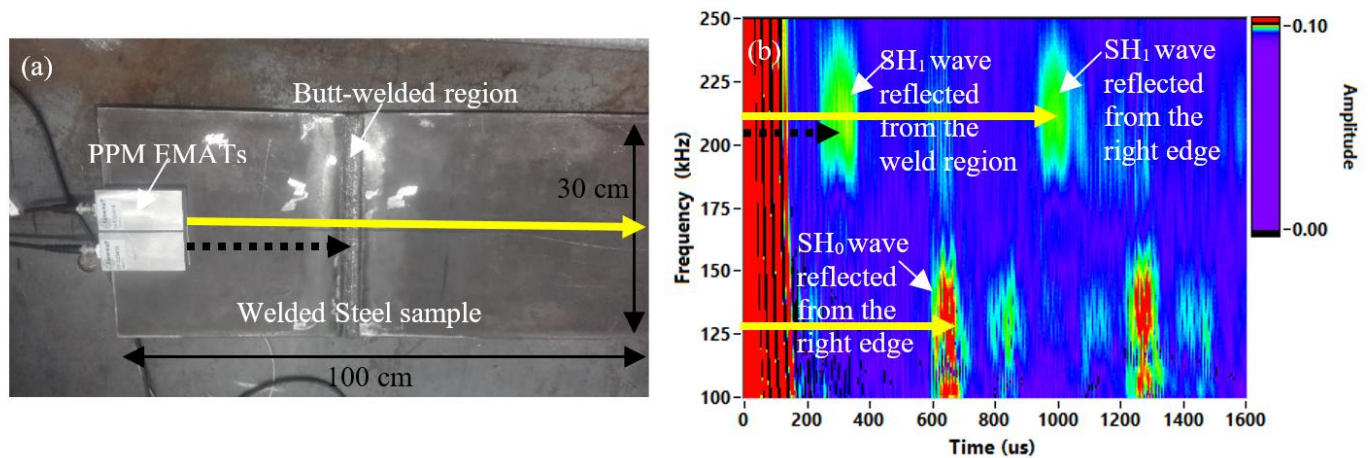

Fig. 12. The sensitivity of SH waves to structural features. (a) EMAT sensors on a 10mm butt-welded mild Steel sample. (b) Sweeping the excitation frequency to identify the sensitivity of both SH_0 and SH_1 wave modes to the edges/welded regions. The propagation paths are shown as dashed black and solid yellow lines.

The excitation frequency of the EMAT generator was swept to generate and evaluate the sensitivity of both SH_0 and SH_1 wavemodes to the features present. The generation of both modes in this frequency range is expected at different frequencies for a fixed wavelength, as shown in Fig. 1. The presence of both modes was confirmed by the data shown in Fig. 12b, which was obtained by stacking up the time traces (A-scans) of the measured signals for different excitation frequencies spanning from 100 kHz-250 kHz. SH_0 is a dominant mode at the range of 100 kHz-175 kHz, whereas, at the range of 175 kHz-250 kHz, SH_1 is the dominant mode.

The source of the reflection for each wave packet in Fig. 12b can be estimated based on the velocity and the propagation distance from the EMAT generator to the welded region and the right edge of the sample, see Fig. 12a.

The reflected echo from the right edge of the sample can be observed at around 600 μs and 100 μs using SH_0 and SH_1 wave modes, respectively, whereas the reflected echo from the welded region can only be revealed when using SH_1, arriving at around 200 μs. This confirmed that the SH_0 wave mode can reveal the boundaries, while the SH_1 can identify both welded regions and boundaries of a component, however, distance determination using the SH_1 mode can be difficult if the sample thickness changes during the wave propagation path and therefore the velocity changes. The reflection from the weld (black path–SH_1) and boundary (yellow path–SH_0 and SH_1) can be clearly seen.

4.2. Experimental validation of GW-OGM

The second experiment was designed to validate the GW-OGM algorithm. Fig. 13 shows the experimental setup on a rectangular 10 mm steel sample with dimensions of 2 x 1 m.
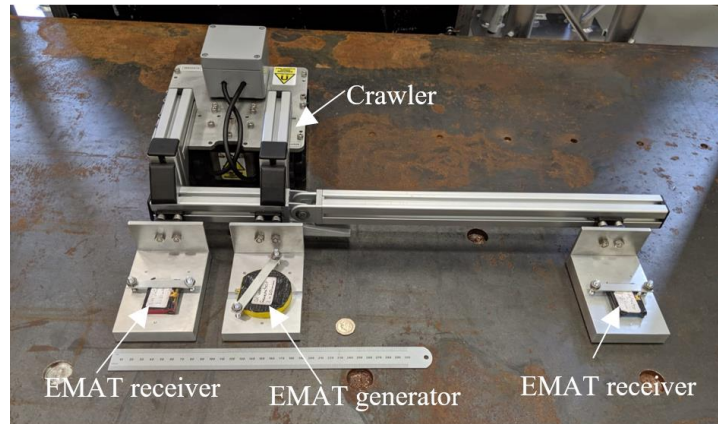

Fig. 13. The crawler [57] equipped with miniaturised EMAT sensors on a 10 mm Steel sample.

EMAT signals were measured at 5 cm intervals using the miniaturised EMAT generator and two receivers [58] with the set-up on the robot shown in Fig. 13. Miniaturised EMATs were used to facilitate ease of scanning, see more details of the fabricated EMAT in ref [50] by authors. It was not possible to scan commercial EMATs due to their strong magnetic attraction to the sample. Fig. 14a shows the map obtained, and confirms that the GW-OGM could successfully map the edges of the sample with an acceptable range measurement error, with error analysis shown in Fig. 14b. Error histogram of range measurements demonstrates that the range accuracy of 1.7 mm can be obtained, which is equivalent to one standard deviation of random errors.
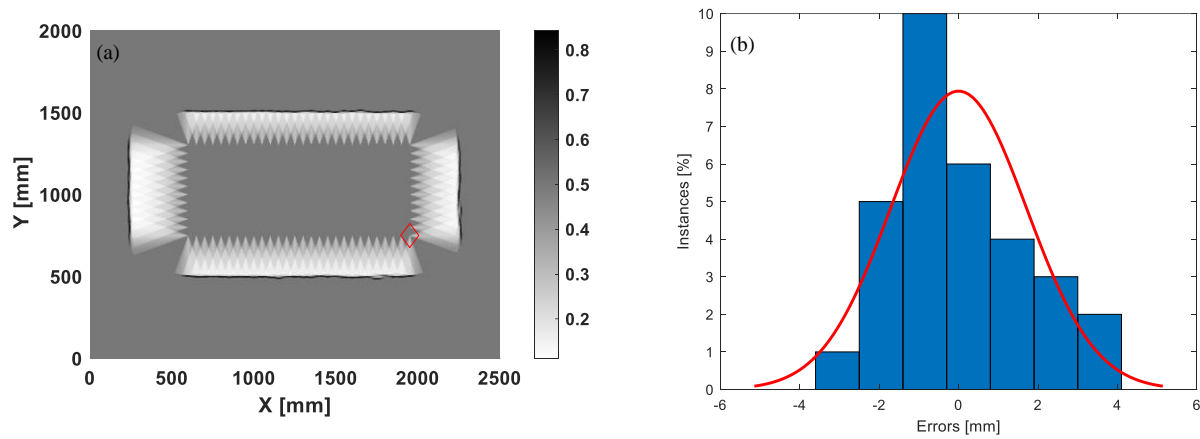
Fig. 14. a) Experimental validation of OGM algorithm on a rectangular 10 mm thick steel plate, b) Error histogram of range measurements with seven bins, showing a range accuracy of <1.7 mm (1σ).

The range accuracy was obtained by comparing the ranges calculated using guided waves with real-world measurements of the sample. The accuracy of our GW-OGM system depends on the ability to extract range data from SH signals and the resolution of grid cells. Unlike the airborne laser scanning systems with an accuracy of ~15 cm [59], the range measured using SH wave modes can provide an accuracy of 1.7 mm once the measurement system is properly calibrated. In order to take full advantage of the accuracy of SH wave modes, the grid cell resolution of 1mm was selected as the effective resolution of the occupancy grid mapping. However, in the existing OGM algorithms, a grid resolution of at least ~10 cm have been reported [60,61].
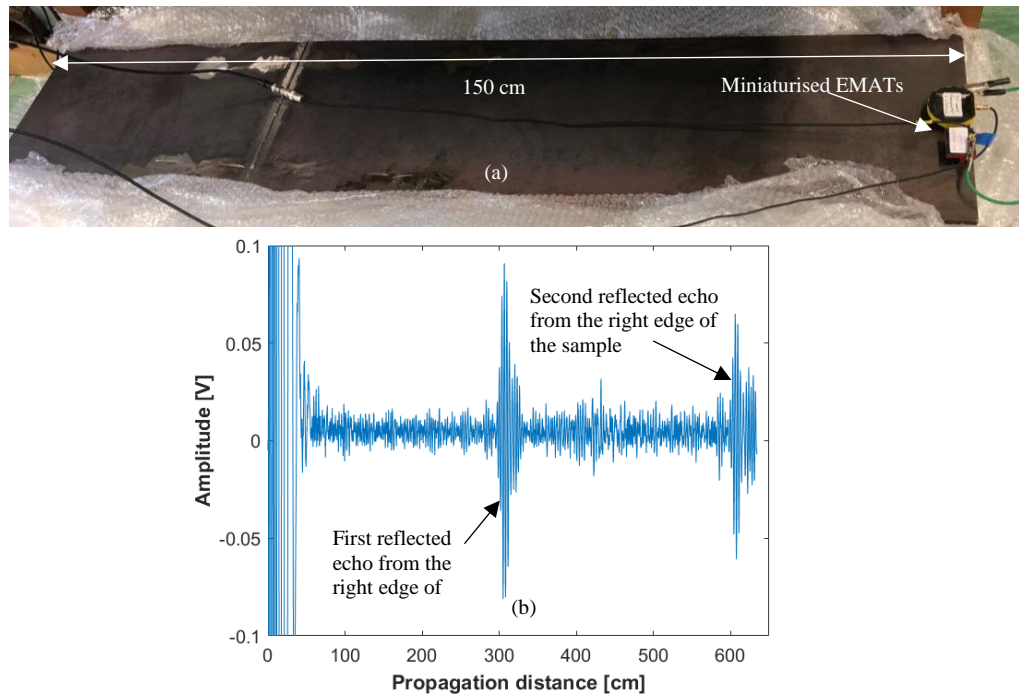

Fig. 15. SH_0 propagation performance of miniaturised EMATs on a 10 mm thick Steel sample measured in a pseudo-pulse-echo mode. (a) Measurement set-up. (b) A typical measured signal.

Only the first echo was evaluated in the experiment as the second echo reflecting from the other side of the sample was difficult to extract due to a reduced signal to noise ratio (SNR) in this sample, possibly due to machined flat bottom holes within the sample. The signals from the miniaturised EMATs have a reduced SNR (~ 30 dB) compared to commercial transducers (~ 36 dB) [50], but waves will propagate over 6 m in samples without multiple defects for an optimised experimental set-up as shown in Fig. 15. It is worth noting that where there is corrosion damage, there is a gradual reduction of wall thickness which will not affect the amplitude of the SH_0 mode significantly [38]. In this case

the mapping range will only be limited by SNR and directionality of the generation of the miniaturised EMATs. The range of the EMATs was measured experimentally by looking at SH_0 mode reflections on an undamaged 10 mm steel plate with 150 cm length. Reflections with high SNR were obtained after the mode had travelled for at least 600 cm.

5. Conclusions

Guided Wave-based Occupancy Grid Mapping (GW-OGM) was investigated in this paper as a first step towards an autonomous robotic ultrasonic inspection for the assessment of industrial structures. Data collection and interpretation was fully automated. However, the robot follows a predefined path and does not currently use the map to plan its trajectory. Integrating automated analysis of the map and then path planning is future work.
GW-OGM was implemented on a 10 mm thick plate-like steel component with irregular geometry in the simulation, showing that it is capable of constructing satisfactory maps with ~1.7 mm accuracy of the geometrical features of the plate, using SH_0 guided waves. Generation and detection of SH wave modes were also confirmed in an experiment on the same material and sample thickness, where the GW-OGM was able to create an estimate of the component's geometry. The maps produced from both simulation and experiment were able to accurately reconstruct the geometries of the inspected plates.

The current GW-OGM takes advantage of an inverse sensor model that assumes that the individual grid cells are independent of their neighbouring cells; this may create some conflicts in the mapping. However, note that this conflict has been significantly compensated in our GW-OGM algorithm as we are using a probabilistic occupancy grid mapping instead of a binary version. In the binary version, two true and false values are used for the occupied and free spaces. Moreover, it has been reported that the "forward sensor model" can be used to mitigate this issue [21], which we will evaluate in the future.

Inspection of large storage tanks as a realistic real-world application scenario can be assumed as inspection of flat sample for the evaluation of guided waves. The main challenge, therefore, is the selection of the wave mode that is the most sensitive wave to all geometrical features and can propagate long-range distances. The experimental measurements confirmed that the SH_0 wave mode is suitable for detecting sample edge features, and it is optimal to use this mode as it is non-dispersive and can propagate further than the dispersive SH_1 wave mode. However, it was demonstrated that the SH_1 wave mode can produce large enough reflections from weld features to identify their presence, unlike the SH_0 wave mode. Therefore, there is a trade-off between the propagation distance and the sensitivity to all geometrical features. Future work is considering using combinations of SH_0 and SH_1 as it increases our sensitivity to both defective regions and geometric boundaries such as welds.

The current paper focuses on the detection of geometrical features such as boundaries/welded regions of a component rather than small defects like corrosion. The next step of our research is to use the pitch-catch measurement for this small size feature detection. Both measurement modes, pseudo-pulse-echo and the pitch-catch modes will eventually be integrated to provide full inspection and mapping of the component using ultrasonic guided waves.

Declaration of Competing Interest

The authors declare that they have no known competing financial interests or personal relationships that could have appeared to influence the work reported in this paper.

Appendix A. Bayes' Theorem

Bayes rule can be intuitively described in terms of updating our belief about a hypothesis H in the light of new data D. In other words, the posterior probability $P(H|D)$ is calculated by multiplying the prior probability $P(H)$ by the likelihood $P(D|H)$, which specifies the conditional probability of data D assuming that H was the case. Therefore, Bayes' theorem allows us to 'invert' conditional probabilities, and can be mathematically expressed as below [42]:

$$P(H|D) = \frac{P(D|H)P(H)}{P(D)},$$ (A.1)

The denominator $P(D)$ just serves to normalize the toral posterior probability to 1.

References

[1]   D. Zonta, B. Glisic, I. Adriaenssens, Value of information: impact of monitoring on decision-making, Struct. Control Heal. Monit. 21 (2014) 1043–1056.
[2]   M. Farley, Best practice in the application of NDT-an update, in: 16th World Conf. NDT (WCNDT), 2004.
[3]   S. Walker, S. Rubin, Integrity Testing of Storage Tank Structure Using Robotic Ultrasound, US 2020/0054379 A1, 2020.
[4]   C.N. Macleod, G. Dobie, S.G. Pierce, R. Summan, M. Morozov, Machining-based coverage path planning for automated structural inspection, IEEE Trans. Autom. Sci. Eng. 15 (2016) 202–213.
[5]   R. Fulbright, L.M. Stephens, SWAMI: An autonomous mobile robot for inspection of nuclear waste storage facilities, Auton. Robots. 2 (1995) 225–235.
[6]   A. Kroll, A survey on mobile robots for industrial inspections, Intell. Auton. Syst. 10, IAS 2008. (2008) 406–414.
[7]   S. Soldan, G. Bonow, A. Kroll, RoboGas Inspector - A mobile robotic system for remote leak sensing and localization in large industrial environments: Overview and first results, in: IFAC Work. Autom. Control Offshore Oil Gas Prod., IFAC, 2012: pp. 33–38.
[8]   D. Lattanzi, G. Miller, Review of robotic infrastructure inspection systems, J. Infrastruct. Syst. 23 (2017) 1–16.
[9]   C. Mineo, S.G. Pierce, P.I. Nicholson, I. Cooper, Robotic path planning for non-destructive testing - A custom MATLAB toolbox approach, Robot. Comput. Integr. Manuf. 37 (2016) 1–12.
[10]   M. Tabatabaeipour, J. Hettler, S. Delrue, K. Van Den Abeele, Visualization of delaminations in composite structures using a baseline-free, sparse array imaging technique based on nonlinear Lamb wave propagation, Acta Acust. United with Acust. 103 (2017) 987–997.
[11]   M. Tabatabaeipour, J. Hettler, S. Delrue, K. Van Den Abeele, Non-destructive ultrasonic examination of root defects in friction stir welded butt-joints, NDT E Int. 80 (2016).
[12]   Scorpion 2 ultrasonic tank shell inspection, https://www.eddyfi.com/en/product/scorpion-2 (accessed May 1, 2020).
[13]   S. Bourne, M. Newborough, D. Highgate, Novel solid contact ultrasonic couplants based on hydrophilic polymers, in: 15th World Conf. Non-Destructive Test., Brescia, 2000.
[14]   G. Dobie, Ultrasonic sensor platforms for non-destructive evaluation, University of Strathclyde, 2010.
[15]   Hexagon manufacturing intelligence, https://www.hexagonmi.com/products/laser-tracker-systems (accessed May 1, 2021).
[16]   J.L. Rose, Ultrasonic guided waves in solid media, Cambridge University Press, 2014.
[17]   E. Monaco, B.N. Daniele, M. Vittorio, F. Ricci, N. Testoni, L. De Marchi, A. Marzani, J. Hettler, M. Tabatabaeipour, S. Delrue, Methodologies for guided wave-based SHM system implementation on composite wing panels: results and perspectives from SARISTU scenario 5, in: Smart Intell. Aircr. Struct., Springer, Cham, 2016: pp. 495–527.
[18]   P. Cawley, M.J.S. Lowe, D.N. Alleyne, B.N. Pavalakovic, P.D. Wilcox, Practical long range guided wave testing: applications to pipes and rails, Mater. Eval. 61 (2003) 66–74.
[19]   G. Dobie, R. Summan, S.G. Pierce, W. Galbraith, G. Hayward, A noncontact ultrasonic platform for structural inspection, IEEE Sens. J. 11 (2011) 2458–2468.
[20]   G. Dobie, S. Gareth Pierce, G. Hayward, The feasibility of synthetic aperture guided wave imaging to a mobile sensor platform, NDT E Int. 58 (2013) 10–17.
[21]   T. Sebastian, Learning occupancy grid maps with forward sensor models, Auton. Robots. 15 (2003) 111–127.
[22]   E. Kaufman, K. Takami, T. Lee, Z. Ai, Autonomous Exploration with Exact Inverse Sensor Models, J. Intell. Robot. Syst. Theory Appl. 92 (2018) 435–452.
[23]   A. Elfes, Sonar-based real-world mapping and navigation, IEEE J. Robot. Autom. 3 (1987) 249–265.
[24]   P. Moravec, A. Elfes, High resolution maps from wide angle sonar, in: IEEE Int. Conf. Robot. Autom., 1985: pp. 116–121.
[25]   Robin Murphy, Introduction to the AI robotics, The MIT Press, 2000.
[26]   S.F.A.E. Wijaya, D.S. Purnomo, E.B. Utomo, M.A. Anandito, Research study of occupancy grid map mapping method on Hector SLAM technique, in: Int. Electron. Symp., 2019: pp. 238–241.
[27]   R. Weston, S. Cen, P. Newman, I. Posner, Probably unknown: Deep inverse sensor modelling radar, in: Int. Conf. Robot. Autom., 2019: pp. 5446–5452.
[28]   P. Moghadam, W.S. Wijesoma, D.J. Feng, Improving path planning and mapping based on stereo vision and lidar, 10th Int. Conf. Control. Autom. Robot. Vision, ICARCV. (2008) 384–389.
[29]   Y. Li, Stereo vision and LIDAR based dynamic occupancy grid mapping : Application to scenes analysis for intelligent vehicles, 2013.
[30]   C. N. MacLeod, R. Summan, G. Dobie, S. G. Pierce, Quantifying and improving laser range data when scanning, IEEE Sens. J. 16 (2016) 7999–8009.
[31]   M. Friedrich, G. Dobie, C.C. Chan, S.G. Pierce, W. Galbraith, S. Marshall, G. Hayward, Miniature mobile sensor platforms for condition monitoring of structures, IEEE Sens. J. 9 (2009) 1439–1448.

[32]   B. Ren, H. Cho, C.J. Lissenden, A guided wave sensor enabling simultaneous wavenumber-frequency analysis for both lamb and shear-horizontal waves, Sensors. 17 (2017).

[33]   S. Choi, H. Cho, M.S. Lindsey, C.J. Lissenden, Electromagnetic acoustic transducers for robotic nondestructive inspection in harsh environments, Sensors. 18 (2018) 1–13.

[34]   M. Hirao, H. Ogi, EMATs for science and industry: Noncontacting ultrasonic measurements, Springer US, 2003.

[35]   P.A. Petcher, S. Dixon, Mode mixing in shear horizontal ultrasonic guided waves, Nondestruct. Test. Eval. 32 (2017) 113–132.

[36]   P.A. Petcher, S. Dixon, Weld defect detection using PPM EMAT generated shear horizontal ultrasound, NDT E Int. 74 (2015) 58–65.

[37]   V. Garcia, C. Boyero, J. Antonio, J. Garrido, Corrosion detection under pipe supports using EMAT medium range guided waves, 19th World Conf. Non Destr. Test. (2016).

[38]   A.C. Kubrusly, M.A. Freitas, J.P. von der Weid, S. Dixon, Interaction of SH guided waves with wall thinning, NDT E Int. 101 (2019) 94–103.

[39]   P. Khalili, P. Cawley, The choice of ultrasonic inspection method for the detection of corrosion at inaccessible locations, NDT E Int. 99 (2018) 80–92.

[40]   M. Tabatabaeipour, O. Trushkevych, G. Dobie, R.S. Edwards, C. Macleod, S.G. Pierce, Guided wave based-occupancy grid robotic mapping, in: Lect. Notes Civ. Eng., Springer International Publishing, 2021: pp. 267–275.

[41]   GUIGUW software, http://www.guiguw.com (accessed May 1, 2021).

[42]   A. Chahbaz, J. Goyette, Guided Lamb waves and L-SAFT processing technique for enhanced detection and imaging of corrosion defects in plates with small depth-to-wavelength ratio, 51 (2004).

[43]   S. Thrun, W. Burgard, D. Fox, Probabilistic robotics, The MIT Press, 2006.

[44]   OnScale software, available: https://onscale.com (accessed May 1, 2020).

[45]   G.L. Wojcik, D.K. Vaughan, N. Abbound, J. J. Mould, Electromechanical modeling using explicit time-domian finite elelemnts, in: IEEE Ultrason. Symp., 1993: pp. 1107–1112.

[46]   G.L. Wojcik, D.K. Vaughan, V. Murray, J. Mould, Time-domain modeling of composite arrays for underwater imaging, in: Ultrason. Symp., 1994: pp. 1027–1032.

[47]   D. Alleyne, P. Cawley, A two-dimensional Fourier transform method for the measurement of propagating multimode signals, J. Acoust. Soc. Am. 89 (1990) 1159–1168.

[48]   A. Sedaghati, F. Honarvar, M. Tabatabaeipour, A.N. Sinclair, Investigation of the scattering of Lamb waves from a generalized circular cavity by using Poisson/Mindlin plate theories and numerical simulation, Proc. Inst. Mech. Eng. Part C J. Mech. Eng. Sci. 234 (2020) 152–170.

[49]   M. Tabatabaeipour, O. Trushkevych, G. Dobie, R.S. Edwards, S. Dixon, C. MacLeod, A. Gachagan, S.G. Pierce, A feasibility study on guided wave- based robotic mapping, IEEE Int. Ultrason. Symp. IUS. 2019-Octob (2019) 1567–1570.

[50]   O. Trushkevych, M. Tabatabaeipour, S. Dixon, M.D.G. Potter, G. Dobie, C. Macleod, R.S. Edwards, Miniaturised SH EMATs for fast robotic screening of wall thinning in steel plates, IEEE Sens. J. 21 (2021) 1386–1394.

[51]   T. Yamasaki, S. Tamai, M. Hirao, Arrayed-coil EMAT for longitudinal wave in steel wires, IEEE Ultrason. Symp. (1998) 789–792.

[52]   C. Zhu, M. He, P. Chen, K. Sun, J. Wang, Q. Huang, Navigation for indoor robot: straight line movement via navigator, Math. Probl. Eng. (2018).

[53]   RITEC Inc, http://www.ritecinc.com (accessed May 1, 2021).

[54]   Pico Technology, https://www.picotech.com (accessed May 1, 2021).

[55]   National Instruments, https://www.ni.com/en-gb/shop/labview.html (accessed May 1, 2021).

[56]   Sonemat, https://www.sonemat.co.uk (accessed May 1, 2021).

[57]   Eddyfi Technologies, https://www.eddyfi.com/en (accessed May 1, 2021).

[58]   O. Trushkevych, S. Dixon, M. Tabatabaeipour, G. Dobie, M.D.G. Potter, C. MacLeod, A. Gachagan, S.G. Pierce, R.S. Edwards, Towards guided wave robotic NDT inspection: EMAT size matters, in: IEEE Int. Ultrason. Symp. IUS, 2019.

[59]   S.E. Reutebuch, R.J. McGaughey, H.-E. Andersen, W.W. Carson, Accuracy of a high-resolution lidar terrain model under a conifer forest canopy, Can. J. Remote Sens. 29 (2003) 527–535.

[60]   E. Einhorn, C. Schroter, H.-M. Gross, Finding the adequate resolution for grid mapping - Cell sizes locally adapting on-the-fly, in: IEEE Int. Conf. Robot. Autom., IEEE, Shanghai, China, 2011: pp. 1843–1848.

[61]   Y. Li, Y. Ruichek, Occupancy grid mapping in urban environments from a moving on-board stereo-vision system, Sensors. 14 (2014) 10454–10478.